



Research on keyhole-induced porosity and melt flow kinetic behavior of 2219 alloy T-joint manufactured by dual laser-beam bilateral synchronous welding

Kang Yue¹ · Li Yue¹ · Zhao Yanqiu¹ · Zhan Xiaohong^{1,2}

Received: 3 January 2022 / Accepted: 19 December 2022 / Published online: 26 January 2023
© The Author(s), under exclusive licence to Springer-Verlag London Ltd., part of Springer Nature 2022

Abstract

Based on the dual laser-beam bilateral synchronous welding (DLBSW) of 2219 aluminum alloy T-shaped structure oriented to the needs of aerospace load-bearing structure requirements, the features of the melt pool flow and keyhole induced porosity of DLBSW process are researched in this paper. The surface formation of the melt pool during the welding process was observed and studied by the high-speed camera system. The thermal-fluid coupling modeling and simulation analysis were carried out for the 2219 aluminum alloy T-shaped structure DLBSW process. The temperature field, flow field, and keyhole coupling evolution behavior of the welding process was studied. At the same time, the flow field distribution characteristics of the melt pool surface were induced. Combined with keyhole coupling dynamic behavior, the effect of the driving force of the melt pool on porosity formation was explored, and the three types of porosity caused by keyhole instability during the DLBSW process were revealed.

Keywords Dual laser beam bilateral synchronous welding · 2219 aluminum alloy · T-joint · Keyhole · Fluid flow

1 Introduction

The 2219 aluminum alloy skin-stringer T-shaped structure in the carrier tank is currently mainly manufactured by mechanical processing and riveting technology. However, these processes still have obvious disadvantages such as low efficiency, high labor intensity, and poor fatigue resistance [1–4]. The use of welding technology to reach a dependable connection between the skin and the stringer can effectively overcome these problems, significantly reduce costs, and increase production efficiency, and the weight reduction effect is also significantly improved. Figure 1 shows the schematic diagram of aerospace wall panel structure comparison under different manufacturing technologies.

Dual laser-beam bilateral synchronous welding (DLBSW) technology of skin-stringer T-shaped structure, as a new type of connection technology, has the advantages of concentrated energy density, small welding deformation, and good weld quality. It has received extensive attention from relevant researchers and gradually applied in the aerospace field. The schematic diagram is shown in Fig. 2. It is displayed from the figure that two laser beams and shielding gas nozzle are symmetrically allocated on both sides of the stringer, acting simultaneously on the contact area between the stringer and skin. The base metals in this area are melted to appear a combined melt pool on the underside of the stringer. Then, it cool and solidify to develop the weld seam. The bottom of the skin is not penetrated by the melt pool during the entire welding process, thus ensuring the integrity of the skin to obtain reliable welded components.

At present, the DLBSW technology of aluminum alloy skin-stringer T-shaped structure has been successfully applied in the aviation industries. For example, Airbus in Europe has successfully used this technology in the production of A318 and A380 fuselage panel structures [5, 6]. Application research indicates that the use of the welding technology instead of riveting technology can reduce the weight of components by about 20% and reduce the cost

✉ Zhan Xiaohong
xiaohongzhan_nuaa@126.com

¹ National Key Laboratory of Science and Technology On Helicopter Transmission, Nanjing University of Aeronautics and Astronautics, Nanjing 211106, China

² Aerospace System Engineering Shanghai, Shanghai 200000, China

Fig. 1 The schematic diagram of aerospace wall panel structure comparison under different manufacturing technologies

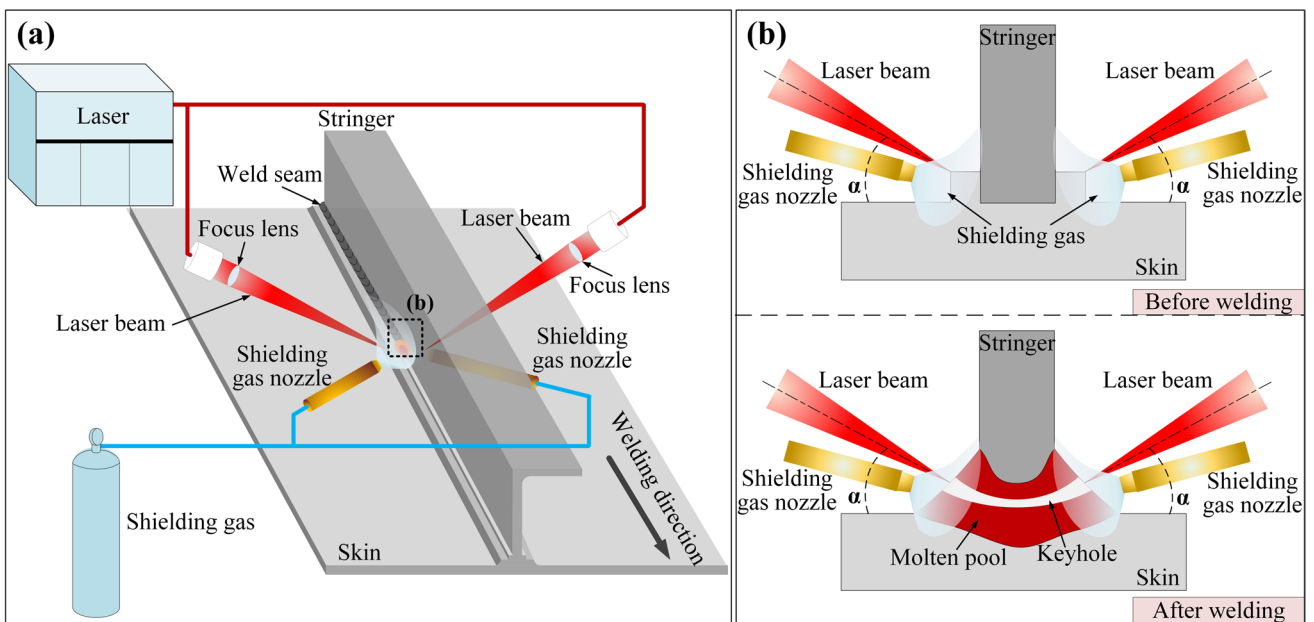
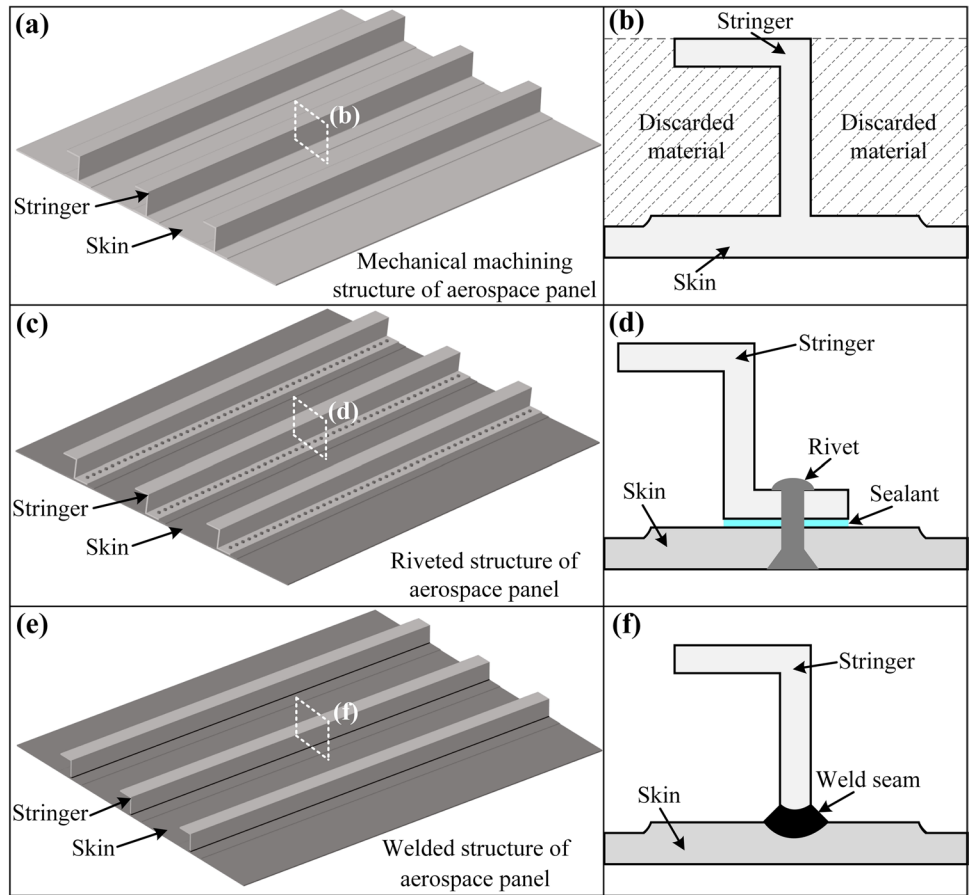


Fig. 2 The schematic diagram of DLBSW process for the aluminum alloy T-joint

by 25% compared with the latter while ensuring reliable service performance [7, 8]. However, DLBSW technology

requires high assembly accuracy for robots, tooling platforms, and welding components; the action of two laser

beams forms a combined melt pool; and its internal metallurgical reaction and flow behavior are complicated. Therefore, in the aerospace field, due to the service characteristics of aerospace carrier components, the technology is still in the pre-research stage, and there are technical problems in equipment, technology, and systems that need to be resolved urgently. In order to overcome these limitations, extensive research has been implemented by research scholars.

Squillace [9] et al. used DLBSW technology to realize the connection of a 3.2-mm thick AA7475 skin with a 2.5-mm thick PA765 stringer T-joint, and researched the effect of different filler materials on its tensile properties. Enz [10] et al. researched the effect of different chemical compositions on the local mechanical properties of CO₂ laser welded T-joints of AA2198 skin and AA2196 beams, such as microhardness and microtensile strength. The results show that the uneven distribution of Li in the weld leads to differences in local hardness and strength. He [11] et al. conducted a 2-mm thick 2060/2099 aluminum–lithium alloy T-joint DLBSW experimental study and analyzed the fracture characteristics of the T-joint under different welding parameters. The study shows that there are obvious dimples at the fracture of the sample, and the average tensile strength of the T-joint in the circumferential and longitudinal directions has reached 80% of the base material. Han [12] et al. used the method of pre-embedded AA4047 welding wire to conduct DLBSW study on 2-mm thick 2060/2099 aluminum–lithium alloy T-joint. The results show that by opening an arc groove on the contact surface of the skin and the stringer to preset the welding wire, a crack-free high-quality aluminum–lithium alloy T-welded joint can be obtained. Oliveira [13] et al. researched the effect of welding parameters on the microstructure and properties of T-joints welded by laser filler wire welding of 2-mm thick AA2024 skin and AA7075 stringers. The influence of process parameters on the macro morphology, microstructure, porosity, and mechanical properties of the T-joint weld is obtained. Chen [14] et al. studied the keyhole coupling and melt flow behaviors of DLBSW process. It involves fluid heat transfer and fluid flow. The results demonstrated that oscillation of the keyhole profile persists both before and after the keyhole coupling.

Based on the above analysis, the current research on DLBSW of aluminum alloy T-shaped structures mainly concentrates on welding experiment and stress-deformation control, but there is a lack of research on the characteristics of the melt pool during the DLBSW process. Therefore, it is taken as the research object in this

paper. It is used the currently developed CFD simulation technology to carry out related research work. Based on the temperature field, morphology and flow field characteristics of the melt pool during the welding process and focus on the growth of porosity induced by keyhole coupling.

2 Experimental procedure

The skin and stringers used in this paper are 2219 aluminum alloy (chemical composition displayed in Table 1), and the thickness of the skin and stringers in the area to be welded is 4.5 mm and 4 mm, respectively. The 3D geometric is displayed in Fig. 3a. In this experiment, two 1.5 mm × 1.5 mm small bosses of equal size, which replace the welding wire filling process, are pre-processed in the welding area on both sides of the stringer and the skin to promote the accuracy and stability of the welding process, as displayed in Fig. 3b. In addition, Fig. 3c and d are the cross-sectional dimensions of the T-shaped structure.

The schematic diagram and field layout of the equipment used in experiment are displayed in Fig. 4. The movement of the laser welding heads on both sides is realized by two robots, and the surface topography of the melt pool during the welding process is photographed by a high-speed camera system. The self-made special welding fixture is used to fix the T-shaped structure during the welding process.

3 Numerical simulation modeling

3.1 Assumptions and governing equations

According to the characteristics of the DLBSW process, the simulation model is partially simplified and assumed under the condition of ensuring the solution accuracy and efficiency, specifically.

- (1) Welding process melt pool of liquid metal for incompressible viscous Newtonian fluid, its flow state for the laminar flow.
- (2) Not considering the effect of the shielding gas on the flow behavior of the melt pool.
- (3) No interpenetration between the melt pool fluids and no consideration of the chemical reactions between the phases.

Table 1 The chemical composition of 2219 aluminum alloy

Element	Cu	Mn	Ti	Zr	V	Zn	Mg	Fe	Si	Al
wt. %	5.8~6.8	0.2~0.4	0.02~0.1	0.1~0.25	0.05~0.15	0.1	0.02	0.3	0.2	Bal

Fig. 3 The geometric diagram and size parameters of 2219 aluminum alloy T-joint

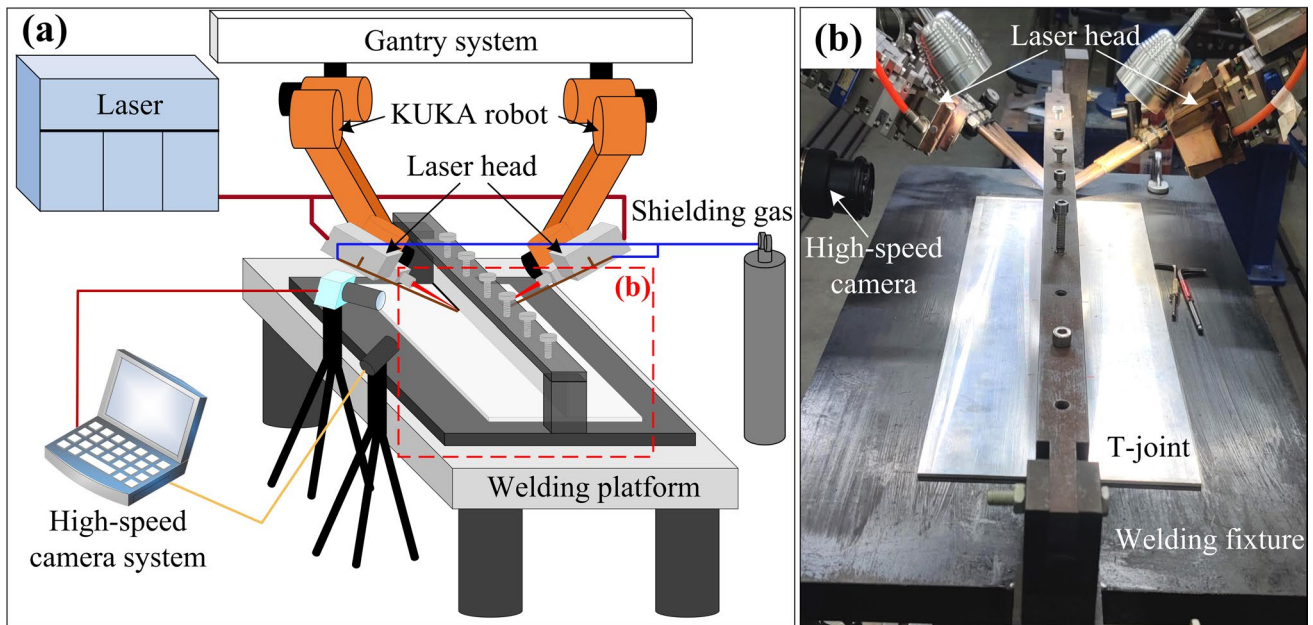
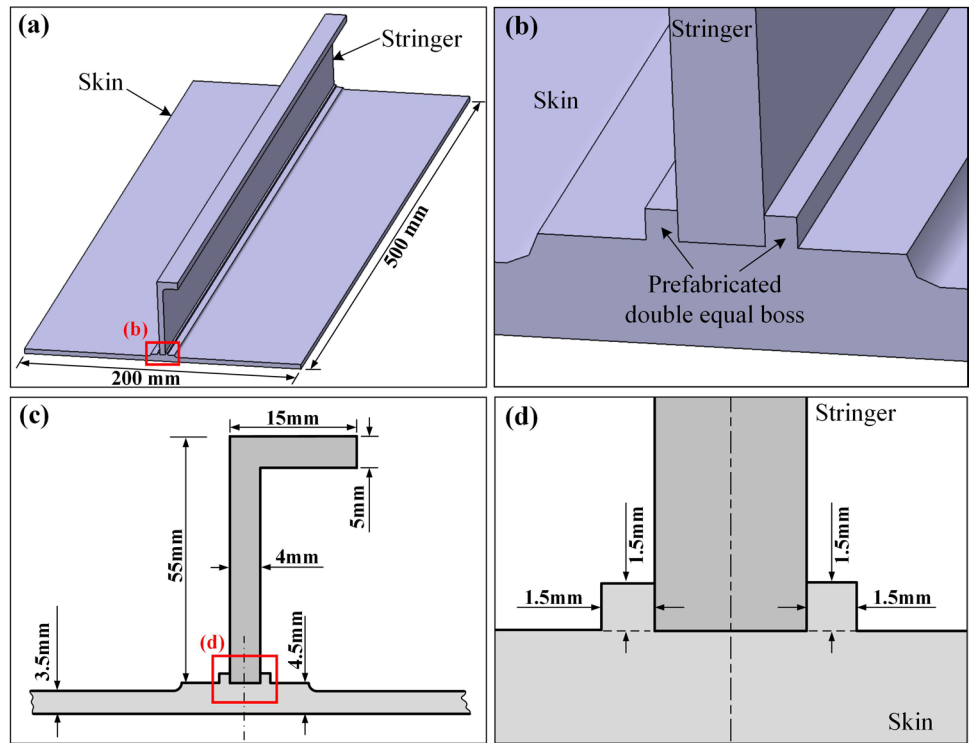


Fig. 4 Schematic diagram and equipment of DLBSW in the experiment

(4) The weld material in the model is considered isotropic, its thermal conductivity and specific heat capacity varies with temperature, and other material performance parameters are set as constants, where the parameters of the solid and liquid phases are different.

In Cartesian coordinate system, the governing equations of fluid flow in DLBSW process are decomposed into mass, momentum, and energy conservation. They are drawn by the following description [14–17]:

Continuity equation:

$$\frac{\partial \rho}{\partial t} + \frac{\partial(\rho u)}{\partial x} + \frac{\partial(\rho v)}{\partial y} + \frac{\partial(\rho w)}{\partial z} = 0 \tag{1}$$

Momentum equation:

X direction:

$$\frac{\partial(\rho u)}{\partial t} + \frac{\partial(\rho uu)}{\partial x} + \frac{\partial(\rho uv)}{\partial y} + \frac{\partial(\rho uw)}{\partial z} = -\frac{\partial P}{\partial x} + \frac{\partial}{\partial x}(\mu \frac{\partial u}{\partial x}) + \frac{\partial}{\partial y}(\mu \frac{\partial u}{\partial y}) + \frac{\partial}{\partial z}(\mu \frac{\partial u}{\partial z}) + S_u \tag{2}$$

Y direction:

$$\frac{\partial(\rho v)}{\partial t} + \frac{\partial(\rho vu)}{\partial x} + \frac{\partial(\rho vv)}{\partial y} + \frac{\partial(\rho vw)}{\partial z} = -\frac{\partial P}{\partial y} + \frac{\partial}{\partial x}(\mu \frac{\partial v}{\partial x}) + \frac{\partial}{\partial y}(\mu \frac{\partial v}{\partial y}) + \frac{\partial}{\partial z}(\mu \frac{\partial v}{\partial z}) + S_v \tag{3}$$

Z direction:

$$\frac{\partial(\rho w)}{\partial t} + \frac{\partial(\rho wu)}{\partial x} + \frac{\partial(\rho wv)}{\partial y} + \frac{\partial(\rho ww)}{\partial z} = -\frac{\partial P}{\partial z} + \frac{\partial}{\partial x}(\mu \frac{\partial w}{\partial x}) + \frac{\partial}{\partial y}(\mu \frac{\partial w}{\partial y}) + \frac{\partial}{\partial z}(\mu \frac{\partial w}{\partial z}) + S_w \tag{4}$$

Energy equation:

$$\frac{\partial(\rho H)}{\partial t} + \frac{\partial(\rho uH)}{\partial x} + \frac{\partial(\rho vH)}{\partial y} + \frac{\partial(\rho wH)}{\partial z} = \frac{\partial}{\partial x}(k \frac{\partial T}{\partial x}) + \frac{\partial}{\partial y}(k \frac{\partial T}{\partial y}) + \frac{\partial}{\partial z}(k \frac{\partial T}{\partial z}) + S_E \tag{5}$$

where u , v , and w are the velocity components in the x , y , and z direction, respectively. ρ is the density of liquid fluid. P is the ambient pressure. μ is the viscosity. k is the thermal

conductivity. H is the mixing enthalpies. S_u , S_v , and S_w are respectively the momentum source terms in the x , y , and z direction. S_E is the energy source term.

In addition, S_u , S_v , S_w , and S_E are the critical factors to calculate the flow field and temperature field in the melt pool and the keyhole dynamic behavior. S_u , S_v , and S_w can be expressed as [18]:

$$S_u = -C \frac{(1-f_L)^2}{f_L^3 + B} (u - u_0) \tag{6}$$

$$S_v = -C \frac{(1-f_L)^2}{f_L^3 + B} v \tag{7}$$

$$S_w = -C \frac{(1-f_L)^2}{f_L^3 + B} w + \rho g \beta (T - T_l) \tag{8}$$

$$f_L = \begin{cases} 0 & T < T_s \\ \frac{T-T_s}{T_L-T_s} & T_s < T < T_l \\ 1 & T > T_l \end{cases} \tag{9}$$

where f_L is the volume fraction of the liquid phase. T_l and T_s are the liquid phase line and solid phase line temperature, respectively. B is a constant. C is the Darcy constant. β is the thermal expansion coefficient. T_l is the liquidus temperature.

S_E could be written as [19]:

$$S_E = Q - m_v L_v - \left[\frac{\partial}{\partial t}(\rho \Delta H) + \frac{\partial}{\partial x}(\rho u \Delta H) + \frac{\partial}{\partial y}(\rho v \Delta H) + \frac{\partial}{\partial z}(\rho w \Delta H) \right] + \frac{\partial}{\partial x}(\rho u_0 \Delta H) \tag{10}$$

where Q is the laser heat source. m_v is the mass transfer. L_v is the latent heat of evaporation.

3.2 Boundary conditions

The surface of the T-joint is characterized by a wall boundary with thermal convection and thermal radiation. The thermal boundary conditions are expressed as:

$$k \frac{\partial T}{\partial \vec{n}} = -h_c(T - T_{ref}) - \varepsilon \sigma (T^4 - T_{ref}^4) \tag{11}$$

where T and T_{ref} are the welding temperature and ambient temperature, respectively. \vec{n} is the normal vector along the wall boundary. h_c is the convection coefficient. ε is the surface radiation emissivity. σ is the Stephan–Boltzmann constant.

3.3 Laser heat source model

In this paper, a combined heat source model is used to simulate the energy transmission of the laser beam, which consists of Gaussian surface heat source and rotating Gaussian body heat source.

The surface heat source model is described as:

$$q_s(x, y) = \frac{\eta_1 Q_s}{\pi r_s^2} \exp\left(-\frac{\alpha(x^2 + y^2)}{r_s^2}\right) \tag{12}$$

where η_1 is the concentration coefficient of the surface heat source. Q_s is the surface heat source effective energy. r_s is the heat source effective radius. α is the correction coefficient.

The body heat source model is described as:

$$q(x, y, z) = \frac{9\eta_2 Q_v}{\pi h r_s^2 (1 - e^{-3})} \exp\left(\frac{-9(x^2 + y^2)}{r_s^2 \ln(h/z)}\right) \quad (13)$$

where η_2 is the concentration coefficient of body heat source. Q_v is the effective energy of body heat source. h is the effective depth of body heat source. In addition, the relationship between the two sub-heat sources can be drawn as follows:

$$Q_\eta = Q_s + Q_v \quad (14)$$

where Q is total laser power. η is the absorptivity of base metal.

In each reflection process, the incident point first absorbs a certain amount of energy, and the remaining energy is the total energy of the next new reflection process. Fresnel absorption is the reflection and energy absorption of laser beam at each point, and the calculation of Fresnel absorption rate is as follows:

$$\alpha(\phi(N)) = 1 - \frac{1}{2} \left(\frac{1 + (1 - \epsilon \cos \phi(N))^2}{1 + (1 + \epsilon \cos \phi(N))^2} + \frac{\epsilon^2 - 2\epsilon \cos \phi(N) + 2(\cos \phi(N))^2}{\epsilon^2 + 2\epsilon \cos \phi(N) + 2(\cos \phi(N))^2} \right) \quad (15)$$

The angle between the laser beam and the normal to the irradiated surface is the reflection angle between the Nth normal of the surface and the Nth incident light, which is the correlation coefficient between the material and the laser type. The value is determined by the laser beam and the material. In this model, the multiple reflections considered in the keyhole are shown in Fig. 5a. The absorption energy after the Nth reflection is calculated as follows [20]:

$$q_N = q_{(N-1)} \alpha(\phi(N)) \quad (16)$$

In Fortran program, each free surface is searched in three-dimensional. In order to achieve multiple reflections, it is necessary to repeatedly search in the search

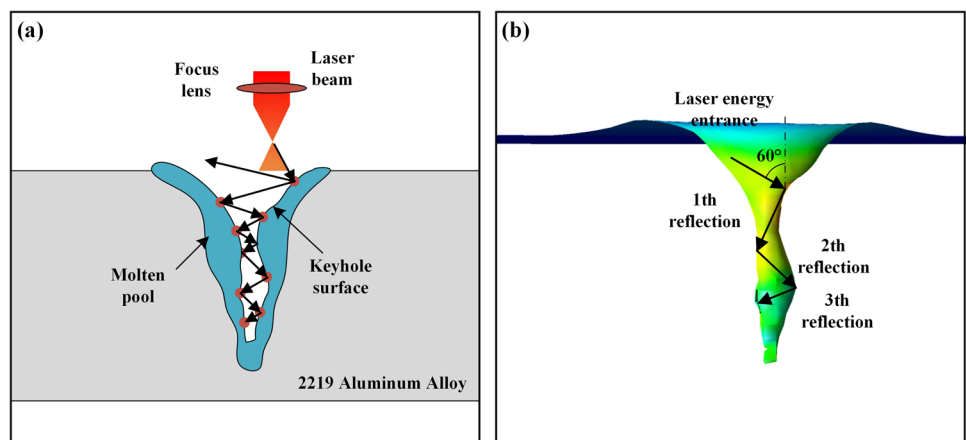
process. For example, during the first search, the first reflection point was determined, and after that, in order to search for the next reflection point and determine the second reflection point, a loop must be performed again at the current progress, so that the R reflection point can be found sequentially. In Fortran loop statements, the method of calling subroutines is usually used for the repeated implementation of the same loop process, mainly because it is difficult to add the same loop to the Fortran loop statements under the same loop. When the same loop process repeats the same loop, it needs to call the subroutine. The verification multiple reflection model is designed as shown in Fig. 5b. The results show that the single-beam laser successfully achieves multiple emission, and each reflection has a certain amount of energy to be attenuated.

3.4 Coordinate system transformation

According to the spatial features of DLBSW, the combined heat sources on the left and right sides of string need to be rotated counterclockwise and clockwise at an angle of θ , respectively. The formula for coordinate transformation can be described as:

$$\begin{cases} x_{rl} = x_l \\ y_{rl} = \cos(\theta)(y - y_l) - \sin(\theta)(z - z_l) \\ z_{rl} = \cos(\theta)(z - z_l) + \sin(\theta)(y - y_l) \end{cases} \quad (17)$$

Fig. 5 Reflection of energy in keyhole during laser welding



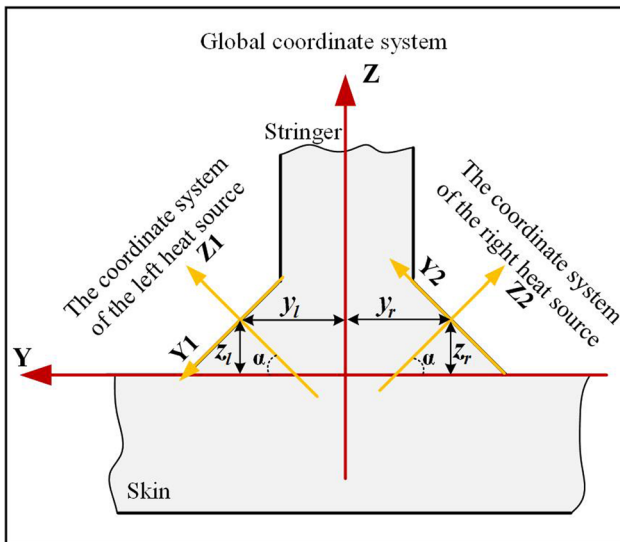


Fig. 6 Schematic diagram of space transformation of heat source coordinate system

$$\begin{cases} x_{rr} = x_r \\ y_{rr} = \cos(\theta)(y - y_r) + \sin(\theta)(z - z_r) \\ z_{rr} = \cos(\theta)(z - z_r) - \sin(\theta)(y - y_r) \end{cases} \quad (18)$$

where x , y , and z are the coordinates before the movement. x_l , y_l , z_l , x_r , y_r , and z_r are the coordinates after the

movement. z_{rl} , y_{rl} , z_{rl} , x_{rr} , y_{rr} , and z_{rr} are the coordinates of after the rotation (Figs. 6, 7 and 8) [14].

3.5 Keyhole surface tracking

The VOF methodology is used to trail the flow physics at the liquid–gas interface [21]. The formula of the methodology is described as:

$$\frac{\partial F}{\partial t} + u \frac{\partial F}{\partial x} + v \frac{\partial F}{\partial y} + w \frac{\partial F}{\partial z} = 0 \quad (19)$$

where u , v , and w are the flow velocities along x , y , and z directions, respectively. If $F=0$, the domain is filled with gas. If $F=1$, the domain is filled with liquid. If $0 < F < 1$, the domain situates on the phase interface of liquid and gas.

3.6 Driving forces

In the simulation, the balance of pressure on the keyhole wall is drawn as follows [22]:

$$P = P_\gamma + P_r + P_g + P_h \quad (20)$$

where P is the total pressure. P_γ is the surface tension. P_r is the vapor recoil pressure. P_g is the hydrostatic pressure. P_h is the hydrodynamic pressure.

The formula of P_h can be described as:

Fig. 7 Schematic diagram of gas–liquid interface reconstruction using young interface reconstruction method

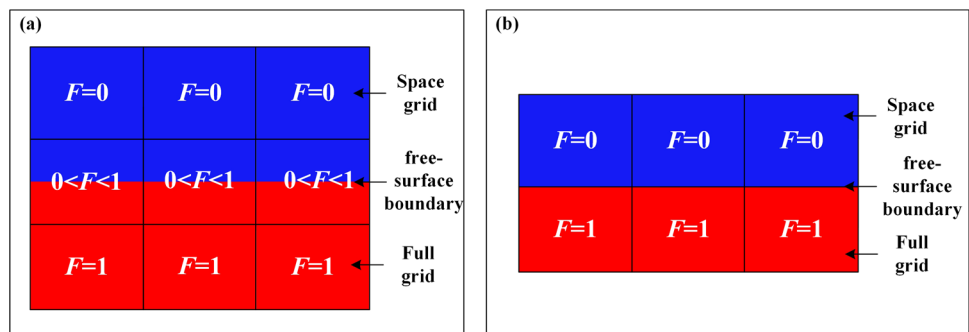
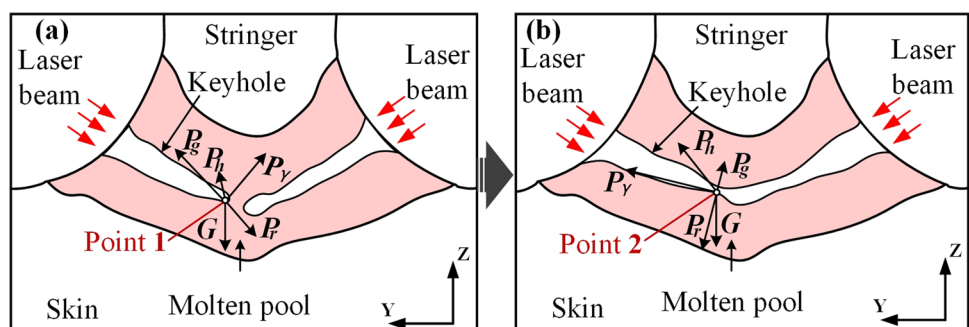


Fig. 8 Diagram of driving force balance on keyhole wall



$$P_r = AB_0 T_w^{-\frac{1}{2}} \exp\left(\frac{-M_a H_v}{N_a k_b T_w}\right) \quad (21)$$

where A is the pressure coefficient. B_0 is the evaporation constant. T_w is the temperature of the keyhole wall. M_a is the atomic mass of the alloy. H_v is the latent heat of evaporation. N_a is Avogadro constant. k_b is the Boltzmann constant.

In addition, the surface tension is described as:

$$P_\gamma = K[\delta_0 + A_\delta(T - T_l)] \quad (22)$$

where K is the free surface curvature related to pressure. δ_0 is the surface tension coefficient. A_δ is the temperature gradient. T_l is the liquid phase line temperature.

Fig. 9 Mesh model and computational domain of the T-joint

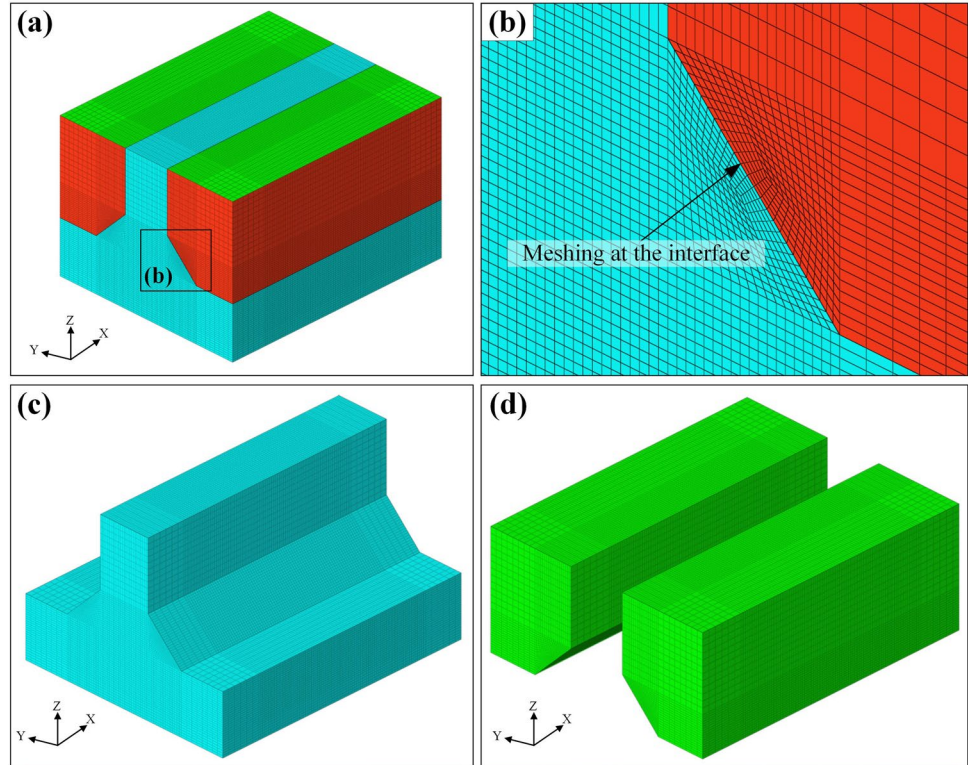


Table 2 Thermal physical properties of 2219 aluminum alloy

Name	Symbol	Unit	Value
Solidus density	ρ_s	kg m^{-3}	2700
Liquidus density	ρ_l	kg m^{-3}	2400
Thermal conductivity of solid	k_s	$\text{W m}^{-1} \text{K}^{-1}$	238
Thermal conductivity of liquid	k_l	$\text{W m}^{-1} \text{K}^{-1}$	100
Specific heat capacity of solid	C_{ps}	$\text{J kg}^{-1} \text{K}^{-1}$	871
Specific heat capacity of liquid	C_{pl}	$\text{J kg}^{-1} \text{K}^{-1}$	1060
Latent heat of fusion	H_m	J kg^{-1}	3.87×10^5
Latent heat of evaporation	H_v	J kg^{-1}	1.08×10^7
Coefficient of surface tension	δ_0	N m^{-1}	0.914
Temperature gradient of surface tension	A_δ	$\text{N m}^{-1} \text{K}^{-1}$	-0.35×10^{-3}
Dynamic viscosity	μ	$\text{kg m}^{-1} \text{s}^{-1}$	0.006
Coefficient of thermal expansion	β		2.36×10^{-5}
Solidus temperature	T_s	K	820
Liquidus temperature	T_l	K	930
Convective heat transfer coefficient	h_c	$\text{W K}^{-1} \text{m}^{-2}$	15
Thermal emissivity	ϵ		0.4
Ambient temperature	T_{ref}	K	300

Table 3 DLBSW process parameters (each side) utilized in simulation and experiment of T-joint

Parameters	Value
Laser power (W)	4400
Welding speed (m/min)	2.1
Laser incidence angle (°)	30
Defocusing amount (mm)	0
Shielding gas flow (L/min)	20

3.7 Computational domain and material properties

A length of 20 mm was chosen as the calculation domain, including both gas phase and solid phases, which is shown in Fig. 9. The main thermal thermophysical properties of 2219 aluminum alloy used in this paper are given by the relevant reference [23] and are shown in Table 2.

Fig. 10 The profile comparison of simulation results and experimental results

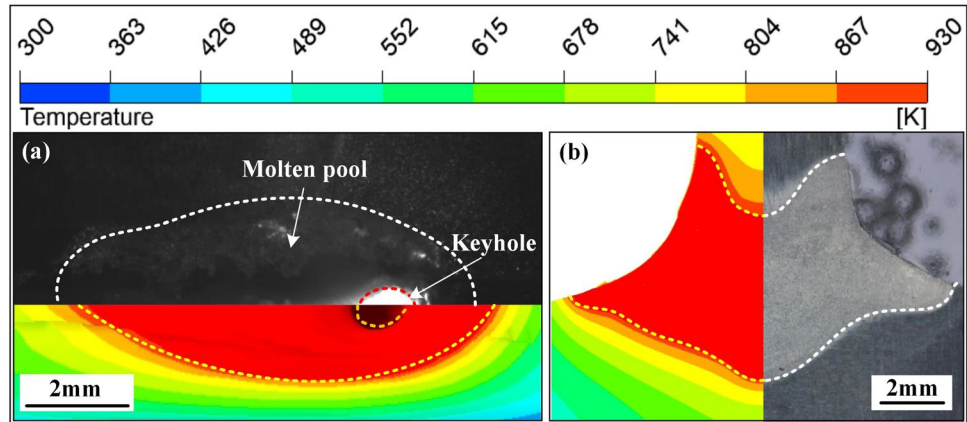
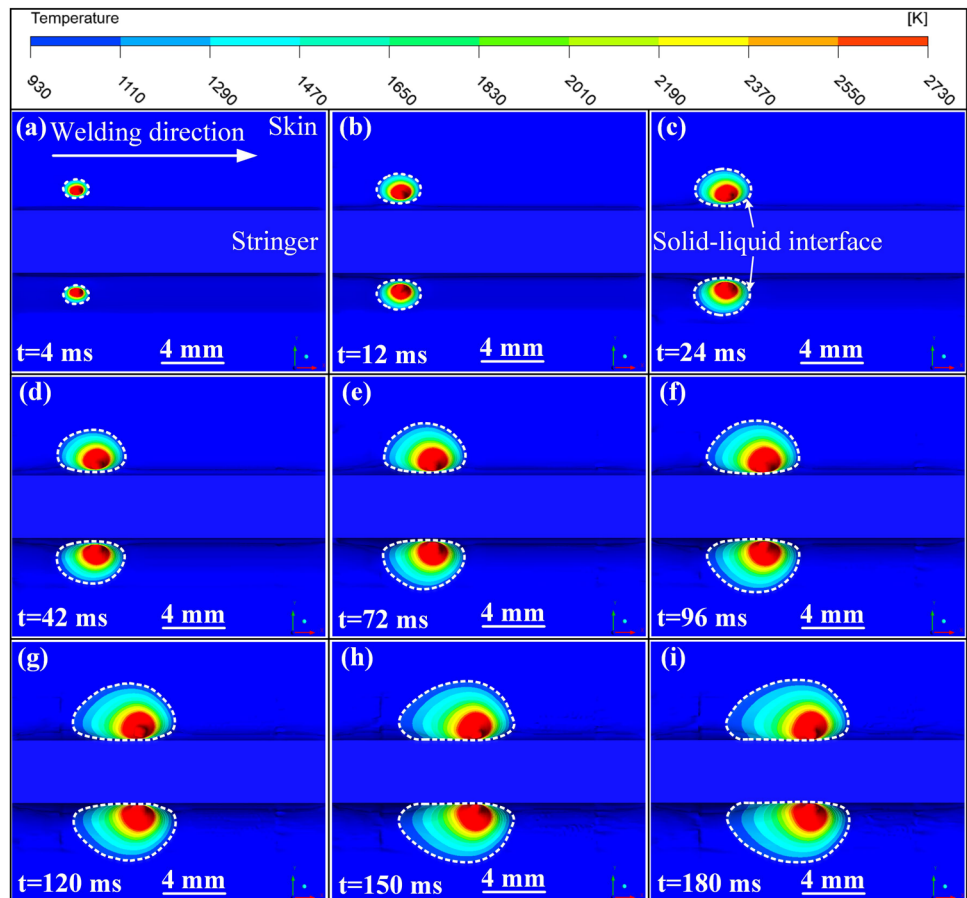


Fig. 11 The temperature field distribution of the melt pool of 2219 aluminum alloy T-joint DLBSW process at different times



4 Results and discussion

4.1 Simulation model validation

The welding process parameters are given in Table 3. Figure 10 clearly displays the calibration of simulation and experimentation results for DLBSW of T-joints.

Figure 10 shows that the results of simulation good match with the results of experimentation. The contours of weld pool and weld are similar in simulation and experiment. It shows that the calculation model is reliable.

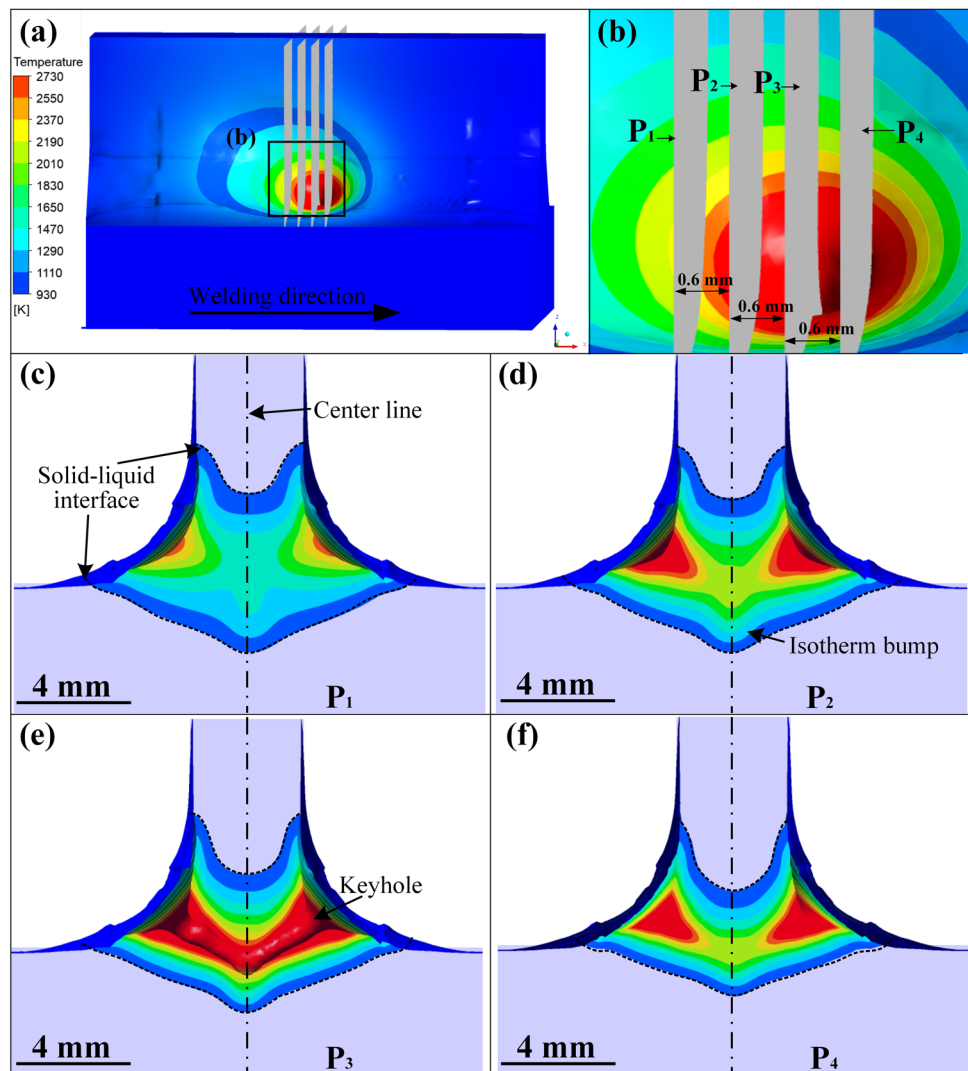
4.2 Temperature field of melt pool

Figure 11 shows the simulation results of the melt pool temperature field distribution (top view) at different times during the welding process. The temperature field of the melt pool on both sides of the stringer is symmetrically distributed and advances in the welding direction synchronously

with the welding process. Between $t = 4$ and $t = 24$ ms, the temperature field of the melt pool presents an approximately circular distribution, the red area is the keyhole and the area near the keyhole. As the welding process progresses, the isotherm behind the temperature field of the melt pool gradually becomes tailed.

The temperature field of the melt pool of different cross-sections in the keyhole and nearby areas perpendicular to the welding direction is shown in Fig. 12. Figure 12c–f are the temperature field distribution results of the P₁–P₄ cross-section respectively. The cross-sectional temperature field is also approximately symmetrically distributed with respect to the beam. The isotherms of the keyhole and the region near the keyhole are distributed in a cone shape along the incident direction of the laser beam from the surface of the T-shaped structure, especially in the keyhole region. The cone-shaped distribution is more prominent. The simulation results show that in the aluminum alloy laser deep penetration welding mode, the laser energy has a certain degree of

Fig. 12 The temperature field distribution results of the melt pool with different cross-sections



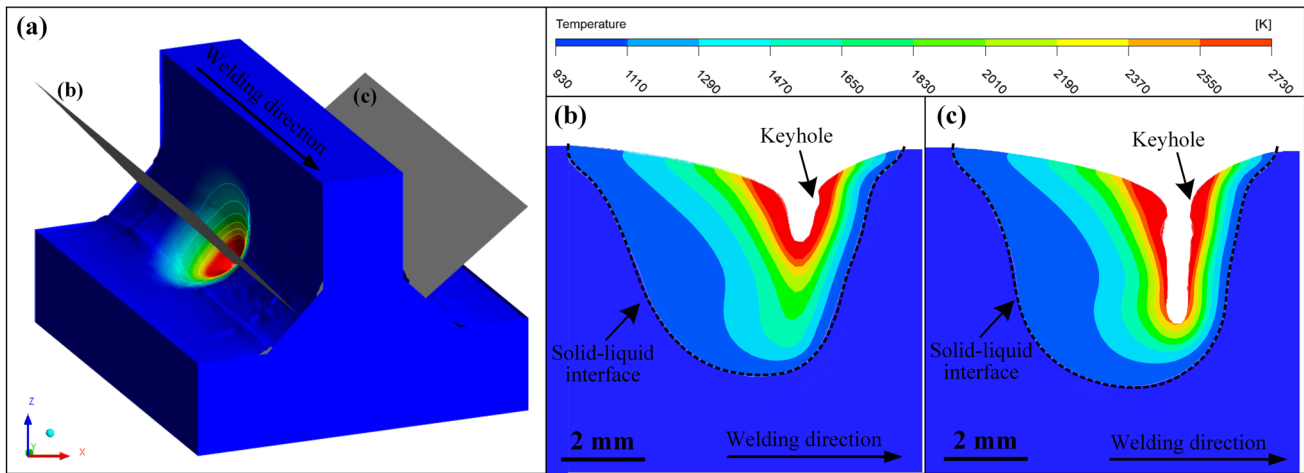


Fig. 13 The temperature field distribution results of the longitudinal section on both sides of the melt pool

attenuation effect in its incident direction, which is in line with the laser energy distribution characteristics of the actual welding process. In addition, the isotherm is obviously convex in the centerline area of the beam, which indicates that there is energy accumulation at the intersection of the laser heat sources on both sides.

The temperature field distribution of the longitudinal section of the melt pool on both sides of the longitudinal beam is further explored, which is shown in Fig. 13. The temperature field distribution characteristics of the longitudinal section of the melt pool on both sides are very analogous. The isotherm of the region near the keyhole wall is also conical from the surface of the melt pool along the direction of the laser heat source. The high temperature area is near the keyhole opening ($T \geq 2550$ K). The range is significantly larger than the bottom of the keyhole. In addition, there is a bulge phenomenon in the isotherm behind the melt pool, that is, the isotherm behind the bottom of the keyhole bulges backward. The characteristic of this isotherm is that there is energy accumulation at the intersection of the laser heat sources on both sides. The heat source moves forward.

4.3 Fluid flow behaviors on melt pool surface

Figure 14 shows the flow field distribution on the surface of the melt pool on both sides of the beam before keyhole coupling. The flow field distribution characteristics on both sides of the melt pool surface are almost the same, and the fluid flow direction on the surface of the melt pool is divergent, flowing from the center of the melt pool to the edge. The fluid velocity at the edge of the melt pool is significantly smaller than that at the center of the melt pool.

Figure 15 shows the flow field distribution results of the weld pool surface on both sides of the longitudinal beam at different times after the keyhole coupling. It can be found

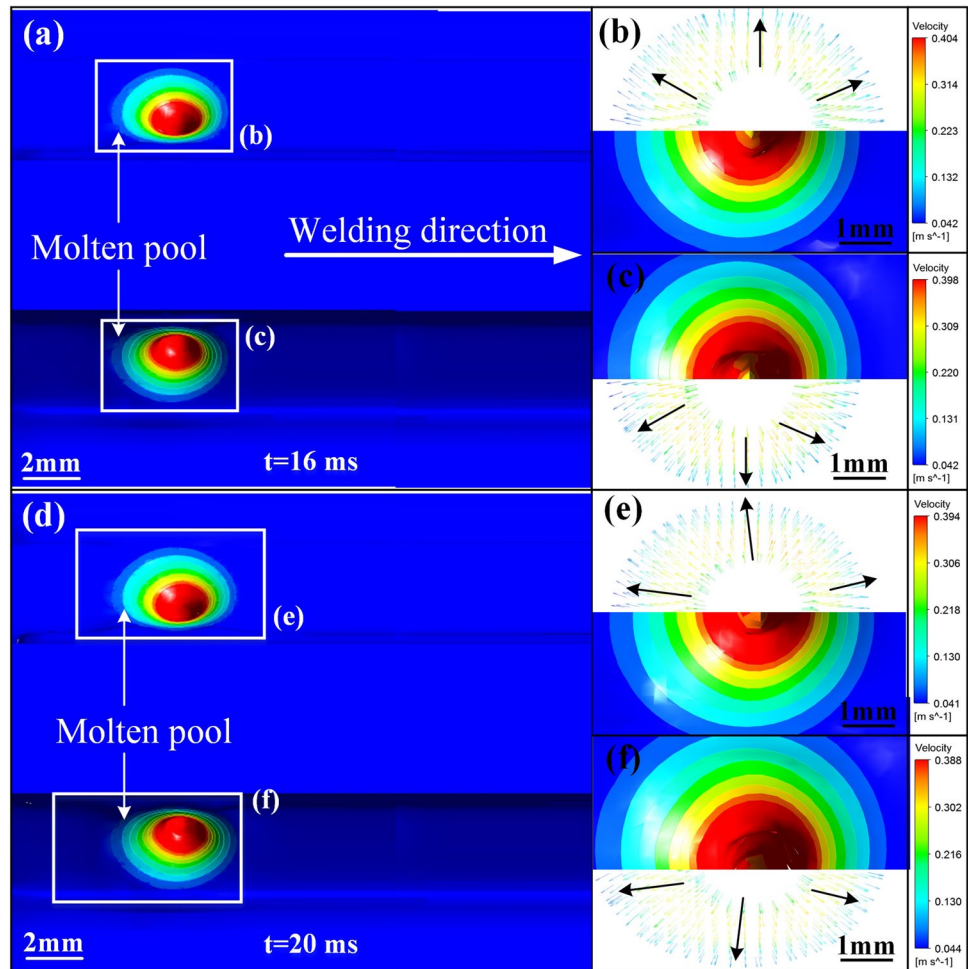
that the fluid flow distribution characteristics on both sides of the weld pool surface are also consistent, and there is a similar flow direction on the weld pool surface before keyhole coupling. In addition, the fluid velocity range on the melt pool surface after keyhole coupling is similar to that before coupling, ranging from $10^{-2} \sim 10^{-1} \text{ m}\cdot\text{s}^{-1}$, and the maximum surface velocity is about $0.4 \text{ m}\cdot\text{s}^{-1}$. Based on the results of the flow field distribution on the surface of the melt pool, it can be seen that there are slight differences in the fluid flow features, flow velocity, and distribution features of the melt pool surface before and after the coupling of small holes.

Figure 16 shows the weld pool morphology at different moments during welding. The surface profile of the melt pool is distributed in a drop shape along the welding direction, from the circular or elliptical shape in the front of the melt pool to the trailing shape in the rear of the melt pool. The relative position of the keyholes in the melt pool area is relatively stable, which are located in the front of the melt pool. This indicates that the spatial position of the weld pool and the keyhole moves relatively stably along the welding direction. In addition, the surface morphology of the weld pool fluctuates continuously during the welding process, and there is a certain degree of depression on the surface of the weld pool.

4.4 Fluid flow behaviors inside melt pool

Subsequently, the fluid flow characteristics of the keyhole wall area before the keyhole coupling were explored, and the result is shown in Fig. 17. When $t = 16$ ms, the fluid velocity distribution on both sides of the keyhole wall is relatively similar, the maximum velocity area is distributed in the keyhole sidewall area, and the maximum velocity reaches $1.073 \text{ m}\cdot\text{s}^{-1}$. The fluid in the lower keyhole wall

Fig. 14 The result of the flow field distribution on the melt pool surface before the keyhole coupling



area has obvious characteristics of flowing along the wall to the bottom end of the keyhole, while the fluid in the upper keyhole wall area has the characteristic of flowing upward from the bottom end of the keyhole along the wall surface. When $t=24$ ms, the fluid in the upper keyhole wall area also shows the phenomenon of flowing along the wall to the bottom of the keyhole, and there is a feature of fluid flowing around the keyhole wall in the area near the opening of the keyhole. At this time, the fluid flow characteristics at the edge of the keyhole opening area are the same as those at $t=16$ ms, and they all flow in a divergent shape to the surrounding area. The maximum flow velocity is $2.428 \text{ m}\cdot\text{s}^{-1}$, which is located in the lower keyhole wall area.

The results of the fluid flow in the keyhole wall area after the keyhole coupling are shown in Fig. 17c and d. When $t=146$ ms, the coupling keyhole has obvious characteristics of fluid flow around the opening. At the bottom of the coupling keyhole, there is a feature of fluid flow upward around the keyhole wall. And there is fluid flowing down the keyhole wall in the upper keyhole wall area. The high fluid velocity area at this moment is principally located at the area

near the opening of the keyhole, and the maximum velocity reaches $2.315 \text{ m}\cdot\text{s}^{-1}$. As the welding process continues, until $t=210$ ms, the flow field distribution in the coupled keyhole wall area is displayed in Fig. 17d. There is fluid flowing upwards along the wall in the upper area of the keyhole. The bottom of the keyhole also has the phenomenon of fluid flowing upwards around the keyhole wall, and near the opening of the keyhole, it is accompanied by fluid flow along the keyhole wall. The characteristics of the fluid flow around it. Additionally, the maximum fluid velocity at this moment reaches $1.505 \text{ m}\cdot\text{s}^{-1}$.

The fluid flow characteristics in the melt pool at $t=210$ ms after keyhole coupling are displayed in Fig. 18. In sections b~d, there is a phenomenon that the front and rear fluids of the melt pool converge on the side of the melt pool near the skin, and then flow to the keyhole wall area, and the top of the keyhole at sections b and d. The fluid has obvious vortex flow characteristics. In section c, the fluid in the edge area of the melt pool flows to the rear of the melt pool along the edge and forms a vortex flow feature above and behind the keyhole. In addition, the large flow rate area at each cross-section is close to the keyhole wall, and the

Fig. 15 The results of the flow field distribution on the melt pool surface after the keyhole coupling

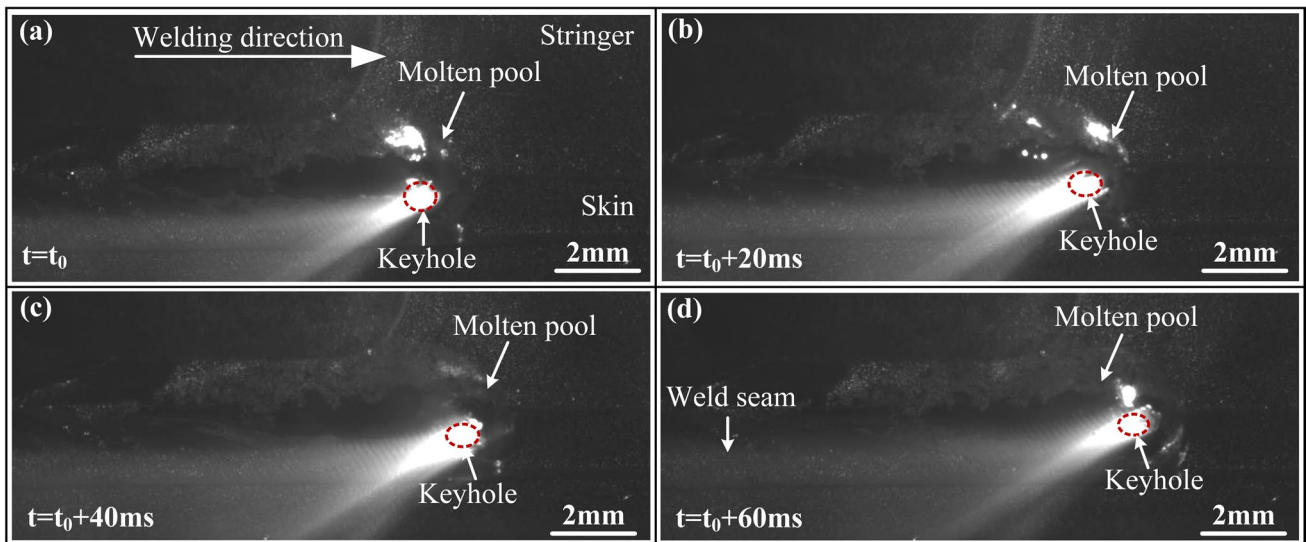
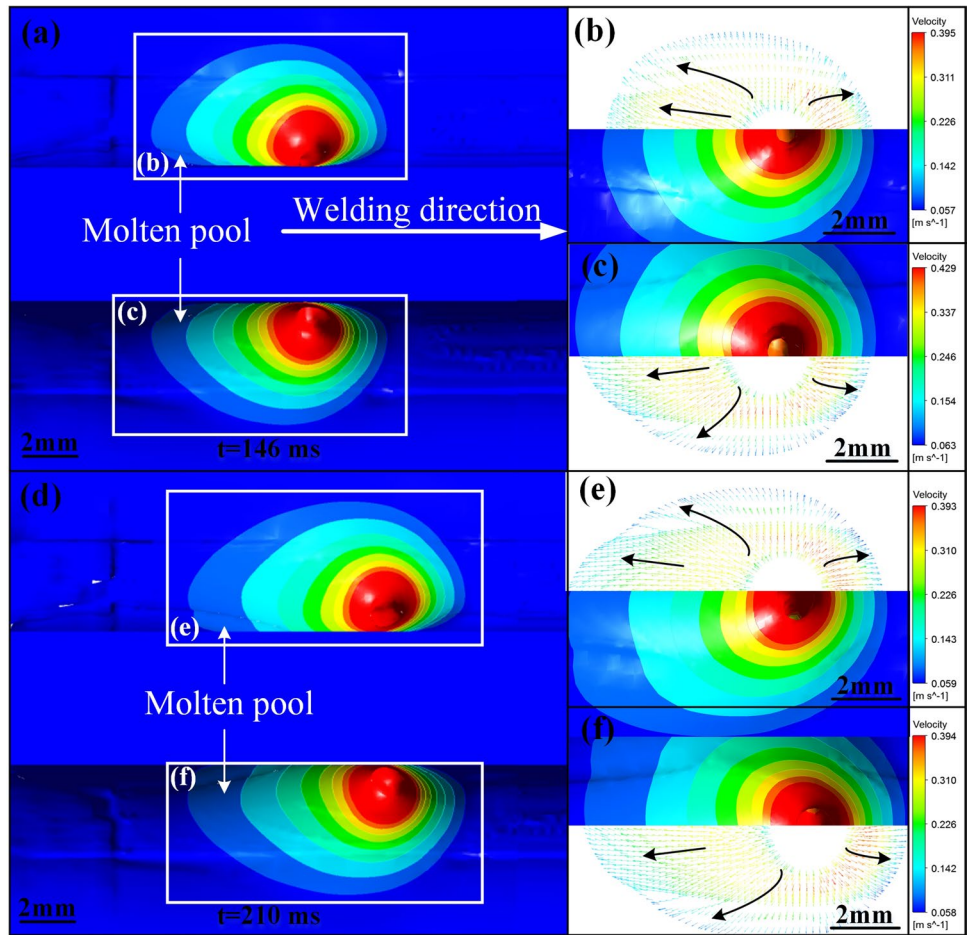


Fig. 16 The morphology of the melt pool at different times during the welding process

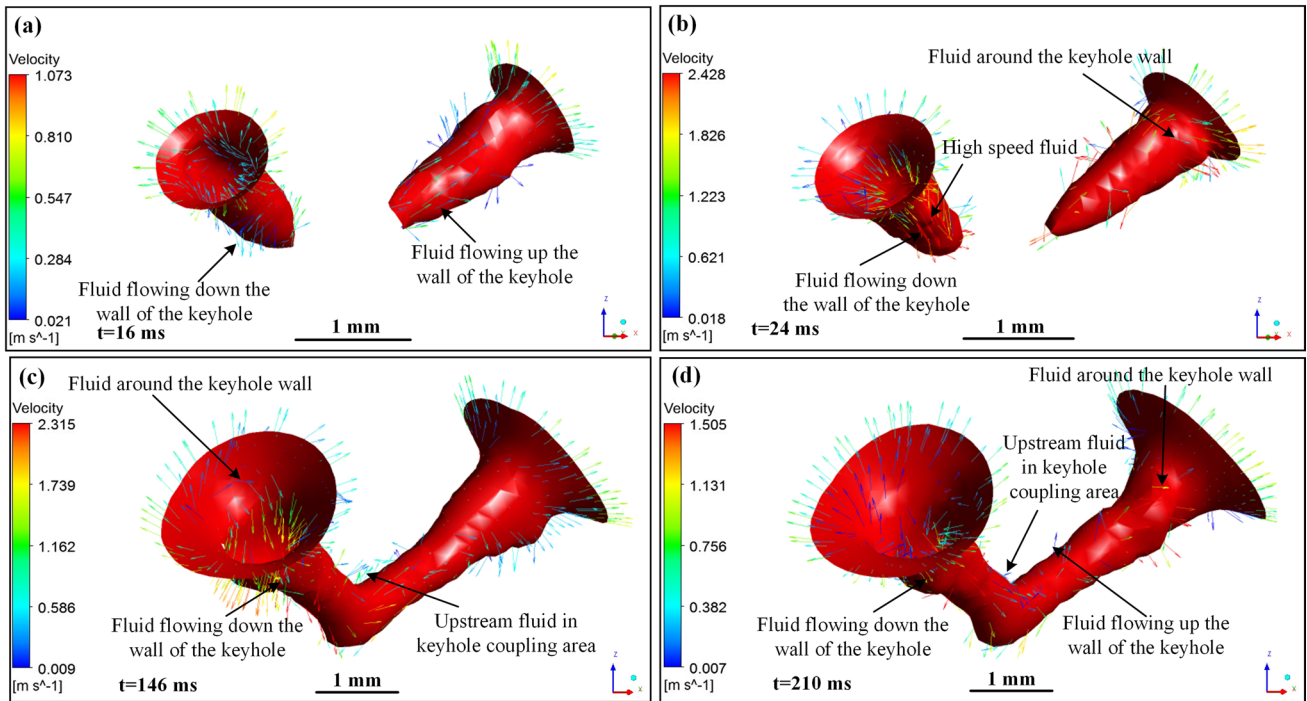


Fig. 17 The flow field distribution of keyhole wall before and after keyhole coupling

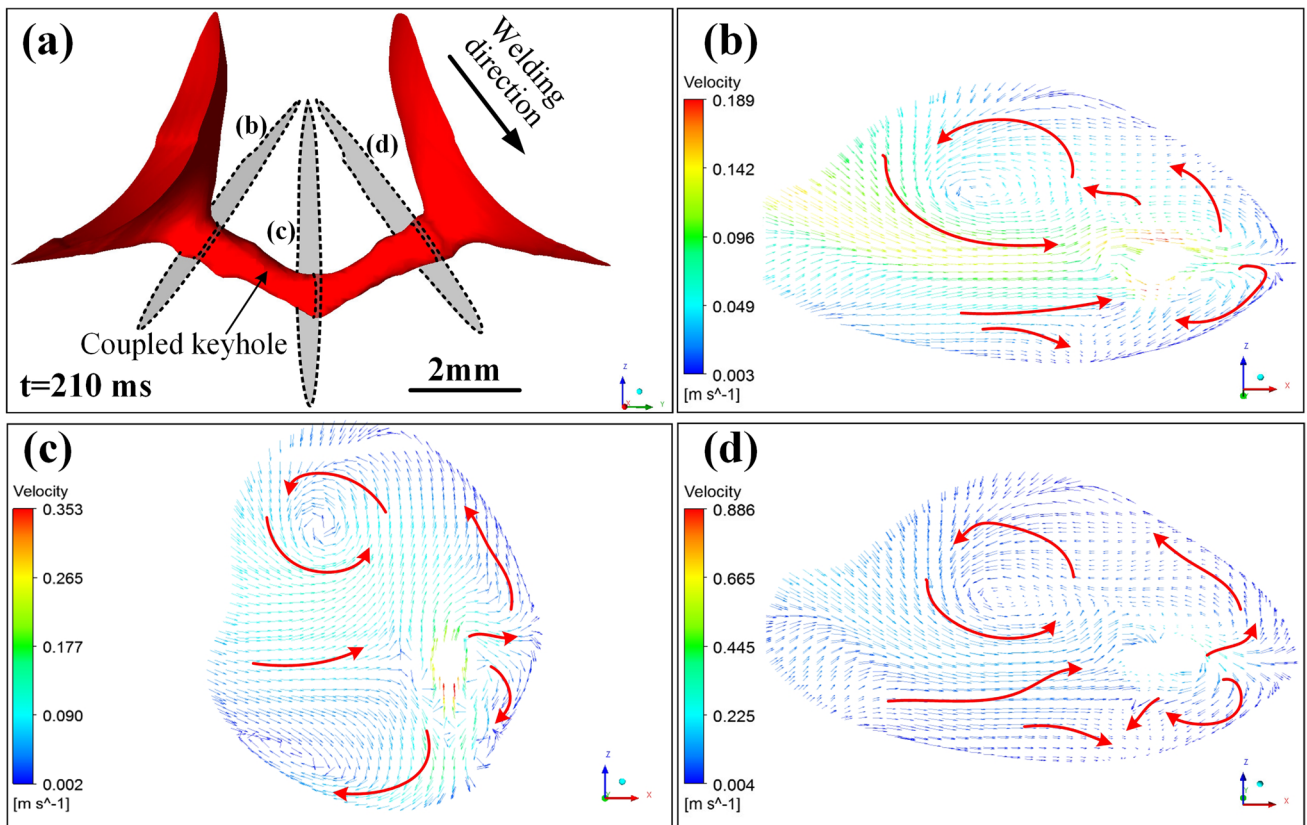
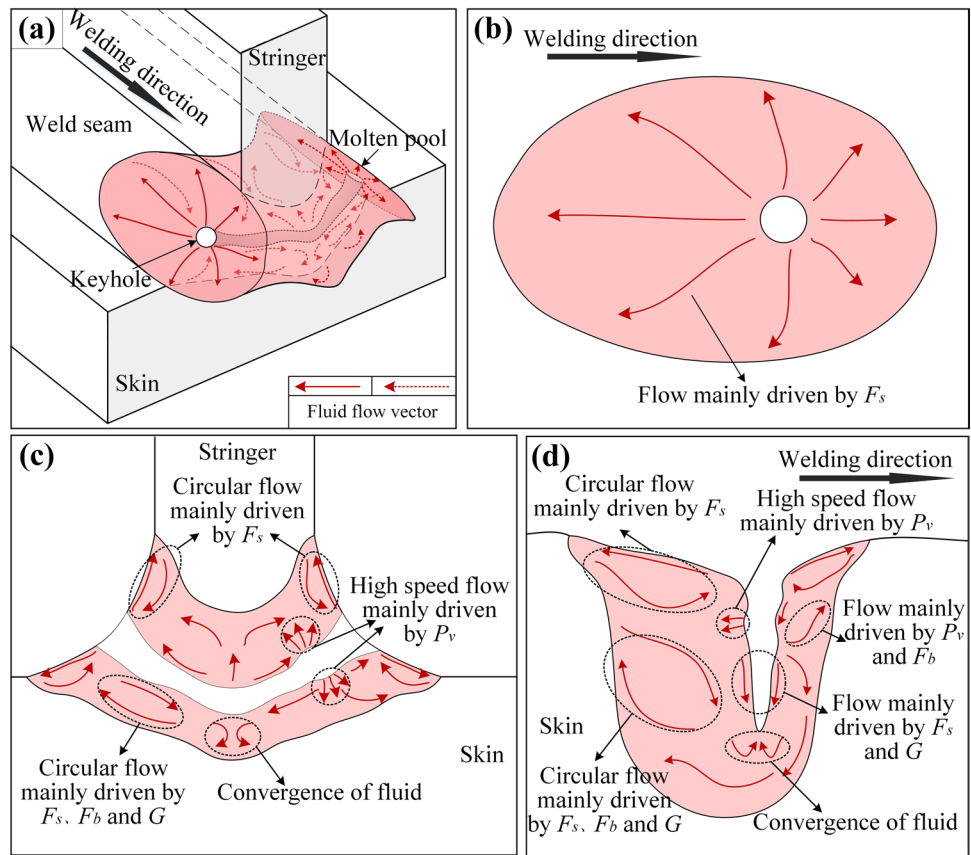


Fig. 18 The internal flow field distribution of the joint melt pool at $t=210$ ms

Fig. 19 The common effect of the driving force of the melt pool on the flow of the 2219 aluminum alloy T-shaped structure in the DLBSW process



fluid flow rate inside the melt pool is significantly smaller than the keyhole wall area.

Figure 19 shows the combined action mechanism of the melt pool driving force on the melt pool flow. Figure 19a is a three-dimensional diagram of the overall flow of the melt pool at a certain moment, and Fig. 19b–d is the corresponding diagram of the fluid flow mechanism of the typical cross section of the melt pool. The fluid on the surface of the melt pool is primarily driven by the surface tension. Under the negative temperature coefficient of the surface tension, the flow fluid of the melt pool surface diverges from the center to the periphery. In the melt pool, the internal fluid flow is more complicated due to the presence of keyholes.

The analysis of the fluid flow mechanism of the cross section and the longitudinal section of the melt pool shows that near the surface of the melt pool, the fluid will flow to the edge of the melt pool under the action of surface tension, and then flow downward, and finally form the Marangoni circulation to the keyhole area. Because the flow range behind the melt pool is bigger, the size of the circulation formed is larger than that on both sides and in front of the melt pool. Due to the effect of the gap pressure, the local area of the hole wall may be concave, and high-speed fluid may be generated in these areas. The high-speed fluid will converge with the fluid inside the melt pool and flow

together to the upper or bottom of the melt pool. The circulation formed at the lower left and back ends of the melt pool is mainly driven by surface tension, thermal buoyancy, and gravity. For fluid flowing upward or downward along the keyhole wall, it is also driven by surface tension, thermal buoyancy, and gravity. In addition, below the keyhole coupling area, the parallel downward flow formed by the collision and convergence of the fluid on both sides is dispersed at the bottom of the melt pool and flows to both sides, flowing along the edge of the melt pool under the combined action of thermal buoyancy and gravity.

In general, due to the volatility of keyhole morphology in the welding process, the flow of the melt pool also has the characteristics of dynamic change. There are some differences in the specific flow characteristics of the melt pool at different times. The dominant driving force of the driving fluid flow area is different, but its driving mechanism for the melt pool flow is the same, which is mainly caused by the combined driving effect of recoil pressure, surface tension, gravity, and thermal buoyancy.

4.5 Keyhole dynamic behavior

The melt pool flow has a great influence on the keyhole stability, as shown in Fig. 20, which is the keyhole collapse

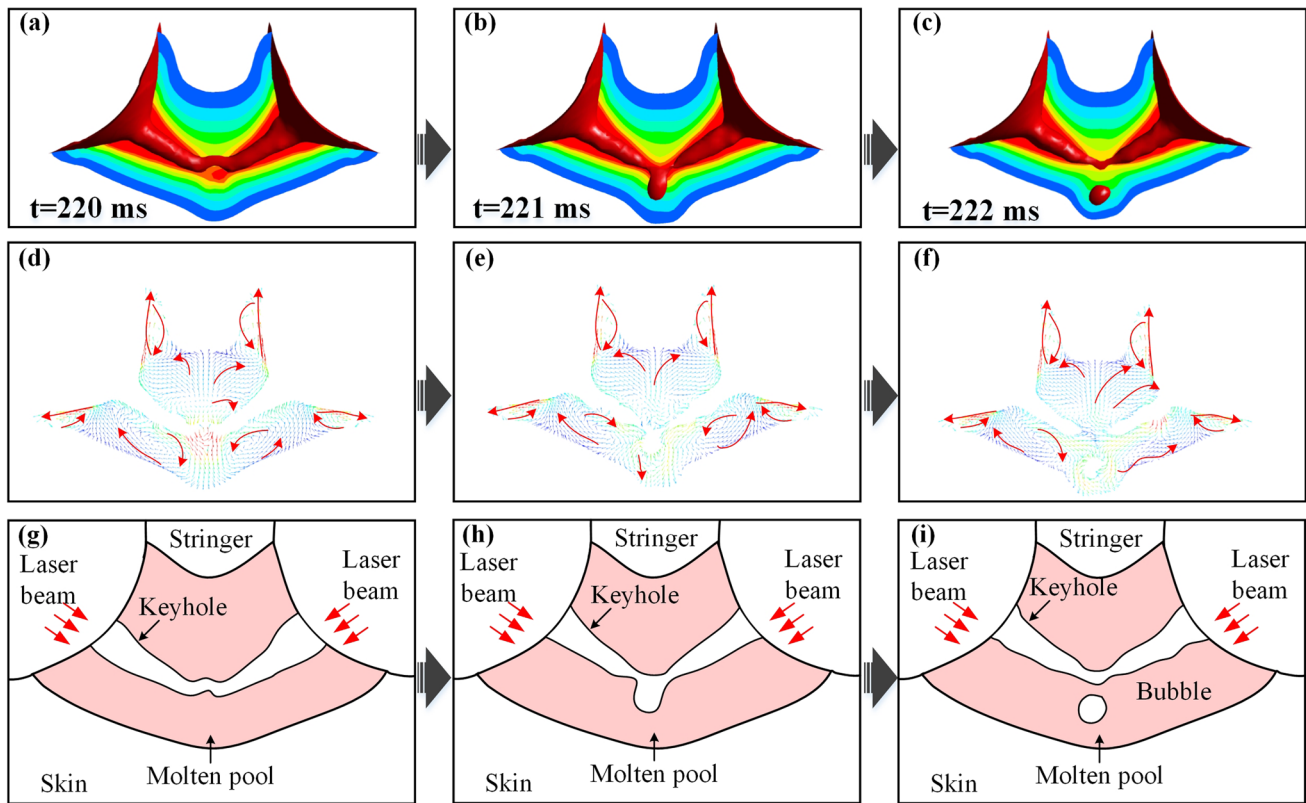


Fig. 20 Bubble formation at bottom of coupling keyhole. (The coupling keyhole is not broken)

process simulation diagram. The increase of energy attenuation in the keyhole coupling region leads to the decrease of temperature at the keyhole coupling region, which leads to the weakening of the recoil pressure in this region, the decrease of the driving force for the outward expansion of the lower wall of the keyhole coupling, and the obvious fluctuation of the keyhole coupling region and the formation of bubbles. This part of the bulge absorbs the direct energy of laser and evaporates strongly. The flow at the coupling keyhole is stronger, and the larger bulge is easier to form at the keyhole coupling region. As the keyhole approaches stability, the bulge formed at the keyhole coupling is formed below the keyhole. The bulge position at the keyhole coupling receives the damage of the melt pool liquid bridge around, and the bottom of the keyhole coupling region collapses. A closed space is separated from the bottom of the keyhole coupling. When this closed space of the coupling keyhole is not destroyed, it will eventually move along the clockwise eddy current to form porosity in the opposite direction of welding.

When the keyhole coupling is relatively stable, the keyhole wall in the keyhole coupling region is approximately parallel to the horizontal plane. Because of the instability of the laser beam on both sides of the stringer, the keyhole coupling region breaks and shrinks at the same

time to form two independent keyholes, and a completely separated keyhole state appears. The tip of the keyhole is easier to close, and the keyhole channel disappears, as shown in Fig. 21, and a bubble is formed below the original keyhole coupling region. The two keyholes are about to be separated, and the flow above the keyhole changes from convection to full flow over the melt pool, which greatly increases the probability of bubbles staying inside the melt pool. When the two side keyholes are completely separated, there is a strong turbulence in the center of the melt pool, which makes the bubbles difficult to escape, and the vortex at the bottom of the keyholes becomes more intense.

When the keyhole coupling is relatively stable, the keyhole wall in the keyhole coupling region is approximately parallel to the horizontal plane. The keyhole is broken in another form of fracture, and the laser beams on both sides of the stringer are symmetrically contracted to form two independent asymmetric keyholes. As shown in Fig. 22, the right keyhole is a relatively stable keyhole, and the left keyhole connecting the convex part of the original coupling keyhole is extremely unstable. Finally, in order to reach a stable state, the tail of the left keyhole is separated separately to form a bubble.

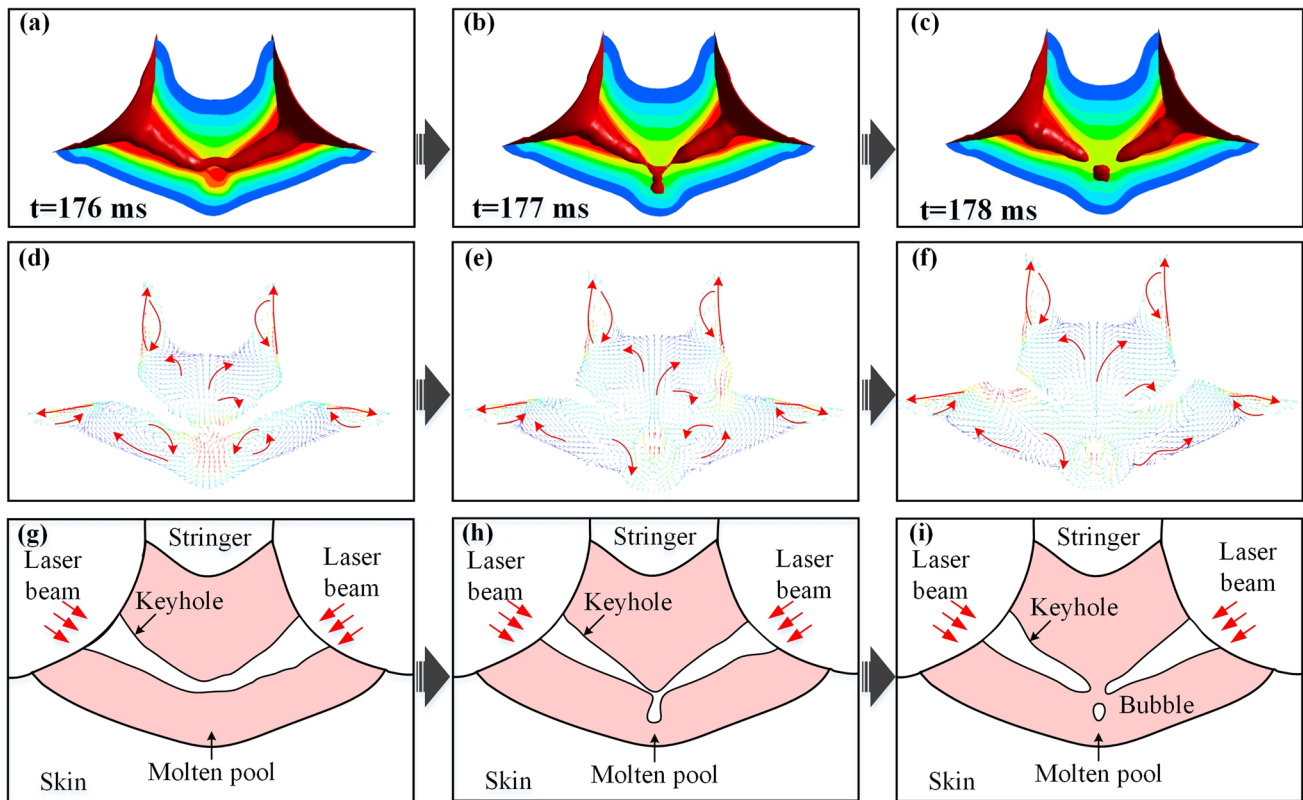


Fig. 21 Bubble formation by coupling keyhole fracture

5 Conclusions

- (1) The fluid on both sides of the melt pool before and after the keyhole coupling flows from the center to the edge of the melt pool, and its velocity gradually decreases from the center to the edge. The maximum surface velocity is about $0.4 \text{ m}\cdot\text{s}^{-1}$.
- (2) The maximum flow velocity of the keyhole wall areas on both sides before the keyhole coupling is distributed at the sidewall of the keyhole. There is fluid flowing along the wall on the sidewall of the keyhole, and the fluid in the opening area of the keyhole flows around in a divergent shape. The flow of liquid metal in the melt pool in the sidewall area of the keyhole is significantly different from that in the keyhole opening area. The fluid in the keyhole wall area after the keyhole coupling has similar flow characteristics before the keyhole coupling, and there is a feature of flowing upward around the keyhole wall in the keyhole coupling area.
- (3) There is Marangoni circulation near the surface of the melt pool, and there are fluid vortex flow characteristics near and behind the keyhole. The maximum flow velocity of the melt pool is about $3 \text{ m}\cdot\text{s}^{-1}$. The accumulation of laser energy causes the fluid flow below the coupling keyhole to be more intense than above it and near the surface of the melt pool.
- (4) Surface tension significantly increases the fluid velocity on the surface of the melt pool and its vicinity and forms Marangoni circulation. The recoil pressure affects the energy absorption mechanism of the melt pool, which increases the volume of the melt pool. The backflushing pressure has a significant effect on the fluid flow inside the melt pool, especially the keyhole wall area, and is the main reason for the high-speed fluid generated in the keyhole wall area.
- (5) There are three forms of porosity formation induced by the coupling keyhole instability as the following: the first is that the unstable coupling keyhole region receives the damage of the melt pool liquid bridge around and forms bubbles staying below the coupling keyhole, and the closed space of coupling keyhole is not destroyed; the second is that the keyhole coupling is relatively stable, but the unstable laser beam on both sides of the stringer leads to the fracture of the coupling keyhole, forming two independent keyholes, and forming bubbles below the original coupling keyhole; and

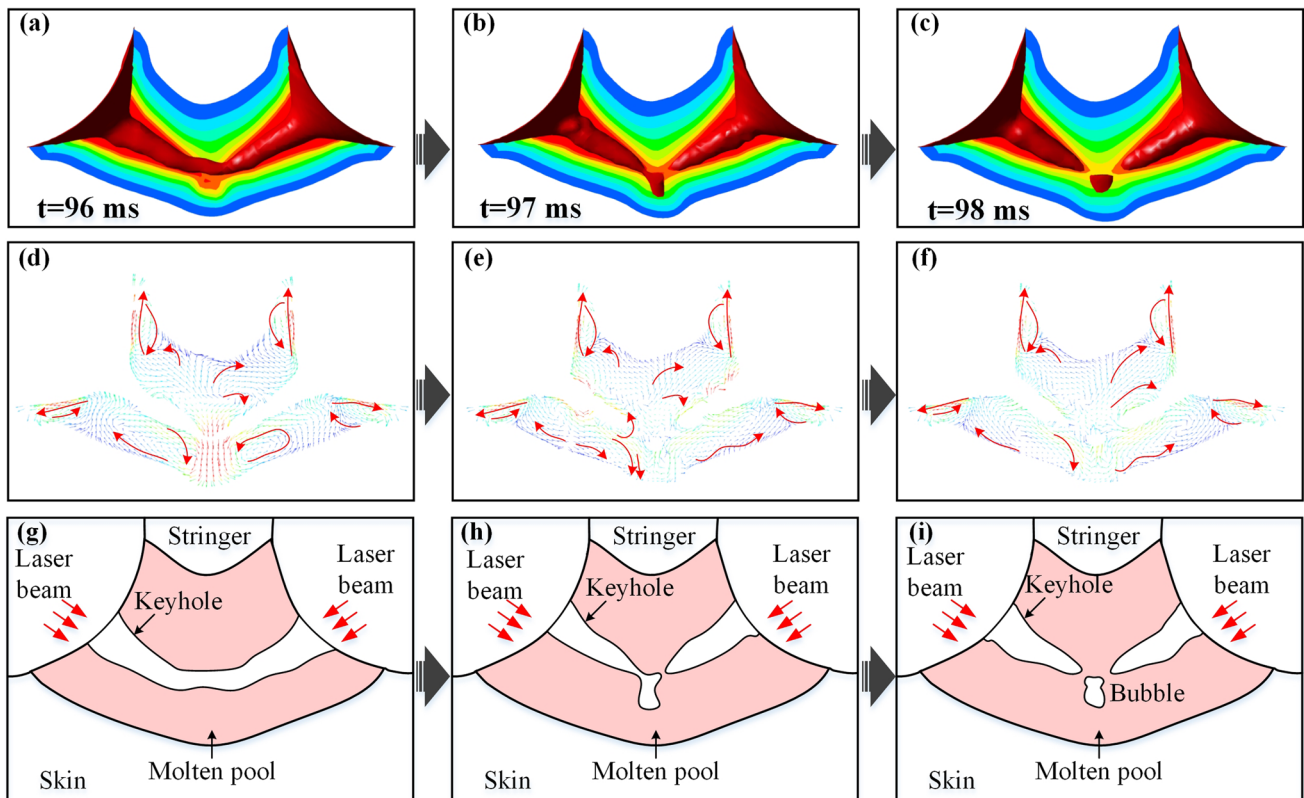


Fig. 22 Unilateral keyhole instability leads to bubble formation after coupling keyhole broken

the third is the coupling keyhole breaks forming two independent and asymmetric keyholes due to the instability of the laser beam on both sides of the stringer, the keyhole on one side is extremely unstable due to the bulge part connecting the original coupling keyhole region, and finally, its tail separates to form a bubble.

Author contribution Yue Kang: investigation, data curation, formal analysis, and writing — original draft. Yue Li: methodology and writing — review and editing. Yanqiu Zhao: writing — review and editing, and validation. Xiaohong Zhan: conceptualization and supervision.

Data availability The raw/processed data required to reproduce these findings cannot be shared at this time as the data also forms part of an ongoing study.

Code availability No supplementary code available.

Declarations

Ethics approval No part of this paper has published or submitted elsewhere. No conflict of interest exists in the submission of this manuscript.

Consent to participate All authors have read and approved this version of the article.

Consent for publication All authors have been taken to ensure the publication of the work.

Conflict of interest The authors declare no competing interests.

References

1. Malarvizhi S, Raghukandan K, Viswanathan N (2008) Effect of post weld aging treatment on tensile properties of electron beam welded aa2219 aluminum alloy. *Int J Adv Manuf Tech* 37(3–4):294–301
2. Ion JC (2000) Laser beam welding of wrought aluminium alloys. *Sci Technol Weld Join* 5(5):265–276
3. Pacchione M, Telgkamp J (2006) Challenges of the metallic fuselage. 25th International Congress of the Aeronautical Sciences-ICAS 4:1–12
4. Vaidya WV, Horstmann M, Seib E, Toksoy K, Koçak M (2006) Assessment of fracture and fatigue crack propagation of laser beam and friction stir welded aluminum and magnesium alloys. *Adv Eng Mater* 8(5):399–406
5. Xia D (1999) Technological research of tank structural material for launch vehicle. *M&SV* 3:32–41
6. Dittrich D, Standfuss J, Liebscher J, Brenner B, Beyer E (2011) Laser beam welding of hard to weld Al alloys for a regional aircraft fuselage design—first results. *Phys Procedia* 12:113–122
7. Li H, Li W, Liu X, Wang Y, Liu Z (2013) Research status and development trend of laser welding technology of plastic. *Adv Mater Res* 753:25–430

8. Wang M (2009) Laser welding technology and aviation manufacturing. *Aeronautical Manuf Technol* 9:48–50
9. Squillace A, Prisco U (2009) Influence of filler material on micro- and macro-mechanical behaviour of laser-beam-welded T-joint for aerospace applications. *Proc Inst Mech Eng L: J Mater: Des Appl* 223(3):103–115
10. Enz J, Riekehr S, Ventzke V, Kashaev N (2012) Influence of the local chemical composition on the mechanical properties of laser beam welded Al-Li alloys. *Phys Procedia* 39(1):51–58
11. He E, Chen L, Wang M (2015) Study on the microstructure and property for T-joints of Al-Li alloy welded by double sided synchronization fiber laser. *Adv Mater Res* 1095:859–864
12. Han B, Tao W, Chen Y (2017) New technique of skin embedded wire double-sided laser beam welding. *Opt Laser Technol* 91:185–192
13. Oliveira PI, Costa JM, Loureiro A (2018) Effect of laser beam welding parameters on morphology and strength of dissimilar AA2024/AA7075 T-joints. *J Manuf Process* 35:149–160
14. Chen S, Zhao Y, Tian S, Yuanzhi Gu, Xiaohong Z (2020) Study on keyhole coupling and melt flow dynamic behaviors simulation of 2219 aluminum alloy T-joint during the dual laser beam bilateral synchronous welding. *J Manuf Processes* 60:200–212
15. Ye XH, Chen X (2002) Three-dimensional modelling of heat transfer and fluid flow in laser full-penetration welding. *J Phys D Appl Phys* 35(10):1049–1056
16. Yang Z, Zhao X, Tao W, Jin C (2019) Effects of keyhole status on melt flow and flow-induced porosity formation during double-sided laser welding of AA6056/AA6156 aluminium alloy T-joint. *Opt Laser Technol* 109:39–48
17. Tao W, Yang ZB, Shi CY, Dong DY (2017) Simulating effects of welding speed on melt flow and porosity formation during double-sided laser beam welding of AA6056-T4/AA6156-T6 aluminum alloy T-joint. *J Alloy Compd* 699:638–647
18. Zhang W, Kim CH, DebRoy T (2004) Heat and fluid flow in complex joints during gas metal arc welding—part I: numerical model of fillet welding. *J Appl Phys* 95(9):5210–5219
19. Voller VR, Prakash C (1987) A fixed grid numerical modelling methodology for convection-diffusion mushy region phase-change problems. *Int J Heat Mass Transf* 30(8):1709–1719
20. Shi L, Li X, Jiang L, Gao M (2021) Numerical study of keyhole-induced porosity suppression mechanism in laser welding with beam oscillation. *Sci Technol Weld Joining* 26(6):1–7
21. Dal M, Fabbro R (2016) An overview of the state of art in laser welding simulation. *Opt Laser Technol* 78:2–14
22. Zhou J, Tsai HL (2008) Modeling of transport phenomena in hybrid laser-MIG keyhole. *Int J Heat Mass Transf* 51(17):4353–4366
23. Faraji AH, Maletta C, Barbieri G, Cognini F, Bruno L (2021) Numerical modeling of fluid flow, heat, and mass transfer for similar and dissimilar laser welding of ti-6al-4v and inconel 718. *Int J Adv Manuf Tech* 114(3):899–914

Publisher's note Springer Nature remains neutral with regard to jurisdictional claims in published maps and institutional affiliations.

Springer Nature or its licensor (e.g. a society or other partner) holds exclusive rights to this article under a publishing agreement with the author(s) or other rightsholder(s); author self-archiving of the accepted manuscript version of this article is solely governed by the terms of such publishing agreement and applicable law.